Static and Dynamic Fracture Analysis for the Interface Crack of Isotropic-Orthotropic Bimaterial

Kwang Ho Lee*

Department of Mechanical Engineering, Sangju National University,
Sangju City, Kyungbuk 742-711, Korea

Arun Shukla, Venkitanarayanan Parameswaran, Vijaya Chalivendra

Department of Mechanical Engineering and Applied Mechanics, University of Rhode Island,
Kingston, RI, 02881, USA

Jae Sug Hawong

Department of Mechanical Engineering, Yeoungnam University, Gyungsan City,
Kyungbuk 712-749, Korea

In the present study, interfacial cracks between an isotropic and orthotropic material, subjected to static far field tensile loading are analyzed using the technique of photoelasticity. The fracture parameters are extracted from the full-field isochromatic data and the same are compared with that obtained using boundary collocation method. Dynamic photoelasticity combined with high-speed digital photography is employed for capturing the isochromatics in the case of propagating interfacial cracks. The normalized stress intensity factors for static cracks are greater when $\alpha=90°$ (fibers perpendicular to the interface) than when $\alpha=0°$ (fibers parallel to the interface), and those when $\alpha=90°$ are similar to ones of isotropic material. The dynamic stress intensity factors for interfacial propagating cracks are greater when $\alpha=0°$ than $\alpha=90°$. For the velocity ranges $(0.1 < c/c_{s1} < 0.7)$ observed in this study, the complex dynamic stress intensity factor $|K_D|$ increases with crack speed c, however, the rate of increase of $|K_D|$ with crack speed is not as drastic as that reported for homogeneous materials.

Key Words : Static and Dynamic Stress Intensity Factor, Interface Crack, Isotropic-Orthotropic Bimaterial Energy Release Rate, Photoelasticity

1. Introduction

Recent years have seen a resurgence of interest in the field of interfacial fracture mechanics due to the oscillatory behavior of stress and displacements as the crack-tip is approached. Interface cracks in view of their importance in numerous applications have received considerable attention in the literature devoted to fracture mechanics (Yang et al., 1991, Deng, 1993, Lee,

* Corresponding Author,
  E-mail : khlee@sangju.ac.kr
  TEL : +82-54-530-5404; FAX : +82-54-530-5401
  Department of Mechanical Engineering, Sangju National University, Sangju City, Kyungbuk 742-711, Korea. (Manuscript **Received** February 6, 2001; **Revised** November 19, 2001)

1999). Gdoutos (Gdoutos et al., 1982) and Lu (Lu et al., 1993) had determined the static stress intensity factors for bimaterial specimens using photoelatiscity. Lambrous and Rosakis (Lambrous et al., 1995a, 1995b) and Kavaturu and Shukla (Kavaturu et al., 1998) have independently proposed fracture criteria for dynamic propagating interfacial cracks.

While the static and dynamic fracture of isotropic-orthotropic bimaterial fracture has extensively been considered theoretically, the experimental investigations of this problem is rather limited. The failure, both static and dynamic, of such interfaces needs to be understood in order to exploit the possibility of bonding together isotropic materials such as metals to orthotropic materials like the fiber

(a) Center Crack Tension (CCT)   (b) Single Edge Crack Tension (SECT)
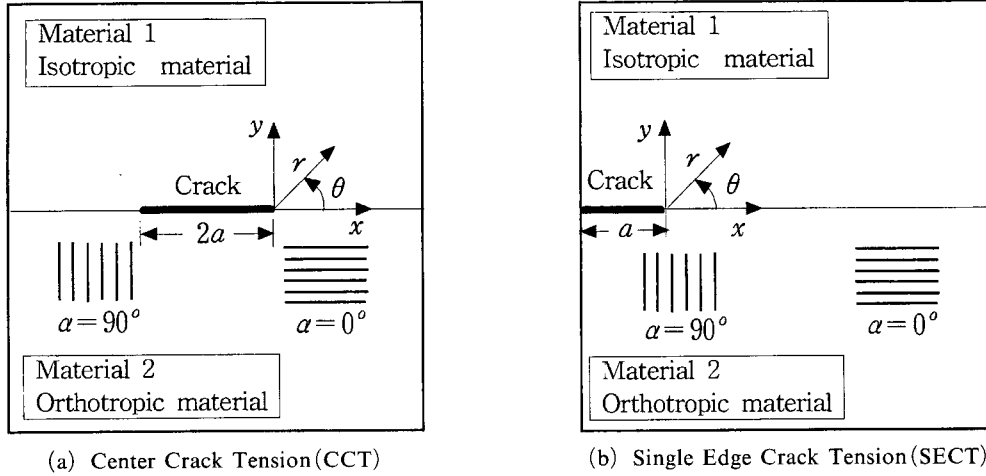
Fig. 1   Interface crack in an isotropic-orthotropic bimaterial

reinforced composites.

In the present study, a detailed experimental investigation is conducted to determine stress intensity factor and energy release rate associated with stationary and propagating cracks along the interface of isotropic-orthotropic bimaterial. High-speed photography coupled with photoelasticity is used to capture the isochromatic fringe pattern. The full field isochromatic data is used to extract the fracture parameters of interest.

2. Stress and Displacement Fields

The oscillatory stress fields (Lee, 1999) with odd power series $(n=1, 3, 5, \cdots)$ for the material above the interface (the isotropic material) in an finite bimaterial (Fig. 1) can be represented as

$$\sigma_{xn} = \sum_{n=odd} \frac{K_n^o}{2\sqrt{2\pi}Dcosh\varepsilon\pi}\left\{-(1+2\beta_l^2-\beta_s^2)\left[e^{\varepsilon(\pi-\theta_l)}\right.\right.$$

$$\overline{A}\cos\left(\varepsilon\ln\frac{r_l}{l}+\frac{n-2}{2}\theta_l\right)-e^{-\varepsilon(\pi-\theta_l)}A\cos\left(\varepsilon\ln\right.$$

$$\left.\left.\frac{r_l}{l}-\frac{n-2}{2}\theta_l\right)\right]r_l^{\frac{n-2}{2}}$$

$$-2\beta_s[e^{\varepsilon(\pi-\theta_s)}\overline{B}\cos\left(\varepsilon\ln\frac{r_s}{l}+\frac{n-2}{2}\theta_s\right)+e^{-\varepsilon(\pi-\theta_s)}$$

$$B\cos\left(\varepsilon\ln\frac{r_s}{l}-\frac{n-2}{2}\theta_s\right)]r_s^{\frac{n-2}{2}}\}$$

$$+\sum_{n=odd}\frac{K_n^*}{2\sqrt{2\pi}Dcosh\varepsilon\pi}\{(1+2\beta_l^2-\beta_s^2)\left[e^{\varepsilon(\pi-\theta_l)}\overline{A}\sin\right.$$

$$\left(\varepsilon\ln\frac{r_l}{l}+\frac{n-2}{2}\theta_l\right)-e^{-\varepsilon(\pi-\theta_l)}A\sin\left(\varepsilon\ln\frac{r_l}{l}-\right.$$

$$\left.\frac{n-2}{2}\theta_l\right)]r_l^{\frac{n-2}{2}}$$

$$+2\beta_s[e^{\varepsilon(\pi-\theta_s)}\overline{B}\sin\left(\varepsilon\ln\frac{r_s}{l}+\frac{n-2}{2}\theta_s\right)+e^{-\varepsilon(\pi-\theta_s)}B$$

$$\sin\left(\varepsilon\ln\frac{r_s}{l}-\frac{n-2}{2}\theta_s\right)]r_s^{\frac{n-2}{2}}\}\tag{1}$$

$$\sigma_{yn}=\sum_{n=odd}\frac{K_n^o}{2\sqrt{2\pi}Dcosh\varepsilon\pi}\{(1+\beta_s^2)\left[e^{\varepsilon(\pi-\theta_l)}\overline{A}\right.$$

$$\cos\left(\varepsilon\ln\frac{r_l}{l}+\frac{n-2}{2}\theta_l\right)-e^{-\varepsilon(\pi-\theta_l)}A\cos\left(\varepsilon\ln\right.$$

$$\left.\left.\frac{r_l}{l}-\frac{n-2}{2}\theta_l\right)\right]r_l^{\frac{n-2}{2}}$$

$$+2\beta_s[e^{\varepsilon(\pi-\theta_s)}\overline{B}\cos\left(\varepsilon\ln\frac{r_s}{l}+\frac{n-2}{2}\theta_s\right)+$$

$$e^{-\varepsilon(\pi-\theta_s)}B\cos\left(\varepsilon\ln\frac{r_s}{l}-\frac{n-2}{2}\theta_s\right)]r_s^{\frac{n-2}{2}}\}$$

$$+\sum_{n=odd}\frac{K_n^*}{2\sqrt{2\pi}Dcosh\varepsilon\pi}\{-(1+\beta_s^2)\left[e^{\varepsilon(\pi-\theta_l)}\overline{A}\right.$$

$$\sin\left(\varepsilon\ln\frac{r_l}{l}+\frac{n-2}{2}\theta_l\right)-e^{-\varepsilon(\pi-\theta_l)}A\sin\left(\varepsilon\ln\right.$$

$$\left.\left.\frac{r_l}{l}-\frac{n-2}{2}\theta_l\right)\right]r_l^{\frac{n-2}{2}}$$

$$-2\beta_s[e^{\varepsilon(\pi-\theta_s)}\overline{B}\sin\left(\varepsilon\ln\frac{r_s}{l}+\frac{n-2}{2}\theta_s\right)+$$

$$e^{-\varepsilon(\pi-\theta_s)}B\sin\left(\varepsilon\ln\frac{r_s}{l}-\frac{n-2}{2}\theta_s\right)]r_s^{\frac{n-2}{2}}\}\tag{2}$$

$$\tau_{xyn}=\sum_{n=odd}\frac{K_n^o}{2\sqrt{2\pi}Dcosh\varepsilon\pi}\{2\beta_l[e^{\varepsilon(\pi-\theta_l)}\overline{A}\sin\left(\right.$$

$$\varepsilon\ln r_l+\frac{n-2}{2}\theta_l\right)+e^{-\varepsilon(\pi-\theta_l)}A\sin\left(\varepsilon\ln r_l-\right.$$

$$\frac{n-2}{2}\theta_l\Big)\Big]r_l^{\frac{n-2}{2}}$$

$$+(1+\beta_s^2)\,[e^{\varepsilon(\pi-\theta_s)}\bar{B}\sin\Big(\varepsilon\ln r_s+\frac{n-2}{2}\theta_s\Big)-$$

$$e^{-\varepsilon(\pi-\theta_s)}B\sin\Big(\varepsilon\ln r_s-\frac{n-2}{2}\theta_s\Big)]r_s^{\frac{n-2}{2}}\Big\}$$

$$+\sum_{n=odd}\frac{K_n^*}{2\sqrt{2\pi}D\cosh\varepsilon\pi}\Big\{2\beta_l[e^{\varepsilon(\pi-\theta_l)}\bar{A}\cos\Big(\varepsilon\ln$$

$$\frac{r_l}{l}+\frac{n-2}{2}\theta_l\Big)+e^{-\varepsilon(\pi-\theta_l)}A\cos\Big(\varepsilon\ln\frac{r_l}{l}-\frac{n-2}{2}$$

$$\theta_l\Big)]r_l^{\frac{n-2}{2}}$$

$$+(1+\beta_s^2)\,[e^{\varepsilon(\pi-\theta_s)}\bar{B}\cos\Big(\varepsilon\ln\frac{r_s}{l}+\frac{n-2}{2}\theta_s\Big)-$$

$$e^{-\varepsilon(\pi-\theta_s)}B\cos\Big(\varepsilon\ln\frac{r_s}{l}-\frac{n-2}{2}\theta_s\Big)]r_s^{\frac{n-2}{2}}\Big\} \quad (3)$$

where $n>0$, n=odd, $A=2\beta_s\eta+(1+\beta_s^2)$, $\bar{A}=2$ $\beta_s\eta-(1+\beta_s^2)$, $B=2\beta_l+(1+\beta_s^2)\,\eta$, $\bar{B}=2\beta_l-(1+\beta_s^2)\,\eta$. Oscillatory displacement fields with odd power series (n=1, 3, 5, ···) for the material above the interface can be represented as

$$u_{xn}=\sum_{n=odd}\frac{K_n^o}{\sqrt{2\pi}(n^2+4\varepsilon^2)\,\mu D\cosh\varepsilon\pi}$$

$$\Big\{-e^{\varepsilon(\pi-\theta_l)}\bar{A}\Big[n\cos\Big(\varepsilon\ln\frac{r_l}{l}+\frac{n}{2}\theta_l\Big)+2\varepsilon\sin\Big(\varepsilon$$

$$\ln\frac{r_l}{l}+\frac{n}{2}\theta_l\Big)\Big]r_l^{\frac{n}{2}}+e^{-\varepsilon(\pi-\theta_l)}A\Big[n\cos\Big(\varepsilon\ln\frac{r_l}{l}$$

$$-\frac{n}{2}\theta_l\Big)+2\varepsilon\sin\Big(\varepsilon\ln\frac{r_l}{l}-\frac{n}{2}\theta_l\Big)\Big]r_l^{\frac{n}{2}}$$

$$-e^{\varepsilon(\pi-\theta_s)}\beta_s\bar{B}\Big[n\cos\Big(\varepsilon\ln\frac{r_s}{l}+\frac{n}{2}\theta_s\Big)+2\varepsilon\sin$$

$$\Big(\varepsilon\ln\frac{r_s}{l}+\frac{n}{2}\theta_s\Big)\Big]r_s^{\frac{n}{2}}-e^{-\varepsilon(\pi-\theta_s)}\beta_sB\Big[n\cos\Big(\varepsilon$$

$$\ln\frac{r_s}{l}-\frac{n}{2}\theta_s\Big)+2\varepsilon\sin\Big(\varepsilon\ln\frac{r_s}{l}-\frac{n}{2}\theta_s\Big)\Big]r_s^{\frac{n}{2}}\Big\}$$

$$+\sum_{n=odd}\frac{K_n^*}{\sqrt{2\pi}(n^2+4\varepsilon^2)\,\mu D\cosh\varepsilon\pi}$$

$$\Big\{e^{\varepsilon(\pi-\theta_l)}\bar{A}\Big[n\sin\Big(\varepsilon\ln\frac{r_l}{l}+\frac{n}{2}\theta_l\Big)-2\varepsilon\cos\Big(\varepsilon\ln$$

$$\frac{r_l}{l}+\frac{n}{2}\theta_l\Big)\Big]r_l^{\frac{n}{2}}-e^{-\varepsilon(\pi-\theta_l)}A\Big[n\sin\Big(\varepsilon\ln\frac{r_l}{l}$$

$$-\frac{n}{2}\theta_l\Big)-2\varepsilon\cos\Big(\varepsilon\ln\frac{r_l}{l}-\frac{n}{2}\theta_l\Big)\Big]r_l^{\frac{n}{2}}$$

$$+e^{\varepsilon(\pi-\theta_s)}\beta_s\bar{B}\Big[n\sin\Big(\varepsilon\ln\frac{r_s}{l}+\frac{n}{2}\theta_s\Big)-2\varepsilon\cos$$

$$\Big(\varepsilon\ln\frac{r_s}{l}+\frac{n}{2}\theta_s\Big)\Big]r_s^{\frac{n}{2}}+e^{-\varepsilon(\pi-\theta_s)}\beta_sB\Big[n\sin\Big(\varepsilon$$

$$\ln\frac{r_s}{l}-\frac{n}{2}\theta_s\Big)-2\varepsilon\cos\Big(\varepsilon\ln\frac{r_s}{l}-\frac{n}{2}\theta_s\Big)\Big]r_s^{\frac{n}{2}}\Big\} \quad (4)$$

$$u_{yn}=\sum_{n=odd}\frac{K_n^o}{\sqrt{2\pi}(n^2+4\varepsilon^2)\,\mu D\cosh\varepsilon\pi}$$

$$\Big\{e^{\varepsilon(\pi-\theta_l)}\beta_l\bar{A}\Big[n\sin\Big(\varepsilon\ln\frac{r_l}{l}+\frac{n}{2}\theta_l\Big)-2\varepsilon\cos\Big(\varepsilon$$

$$\ln\frac{r_l}{l}+\frac{n}{2}\theta_l\Big)\Big]r_l^{\frac{n}{2}}+e^{-\varepsilon(\pi-\theta_l)}\beta_lA\Big[n\sin\Big(\varepsilon$$

$$\ln\frac{r_l}{l}-\frac{n}{2}\theta_l\Big)-2\varepsilon\cos\Big(\varepsilon\ln\frac{r_l}{l}-\frac{n}{2}\theta_l\Big)\Big]r_l^{\frac{n}{2}}$$

$$+e^{\varepsilon(\pi-\theta_s)}\bar{B}\Big[n\sin\Big(\varepsilon\ln\frac{r_s}{l}+\frac{n}{2}\theta_s\Big)-2\varepsilon\cos$$

$$\Big(\varepsilon\ln\frac{r_s}{l}+\frac{n}{2}\theta_s\Big)\Big]r_s^{\frac{n}{2}}-e^{-\varepsilon(\pi-\theta_s)}B\Big[n\sin\Big(\varepsilon$$

$$\ln\frac{r_s}{l}-\frac{n}{2}\theta_s\Big)-2\varepsilon\cos\Big(\varepsilon\ln\frac{r_s}{l}-\frac{n}{2}\theta_s\Big)\Big]r_s^{\frac{n}{2}}\Big\}$$

$$+\sum_{n=odd}\frac{K_n^*}{\sqrt{2\pi}(n^2+4\varepsilon^2)\,\mu D\cosh\varepsilon\pi}$$

$$\Big\{e^{\varepsilon(\pi-\theta_l)}\beta_l\bar{A}\Big[n\cos\Big(\varepsilon\ln\frac{r_l}{l}+\frac{n}{2}\theta_l\Big)+2\varepsilon\cos\Big(\varepsilon$$

$$\ln\frac{r_l}{l}+\frac{n}{2}\theta_l\Big)\Big]r_l^{\frac{n}{2}}+e^{-\varepsilon(\pi-\theta_l)}\beta_lA\Big[n\cos\Big(\varepsilon\,l$$

$$n\frac{r_l}{l}-\frac{n}{2}\theta_l\Big)+2\varepsilon\sin\Big(\varepsilon\ln\frac{r_l}{l}-\frac{n}{2}\theta_l\Big)\Big]r_l^{\frac{n}{2}}$$

$$+e^{\varepsilon(\pi-\theta_s)}\bar{B}\Big[n\cos\Big(\varepsilon\ln\frac{r_s}{l}+\frac{n}{2}\theta_s\Big)+2\varepsilon\sin$$

$$\Big(\varepsilon\ln\frac{r_s}{l}+\frac{n}{2}\theta_s\Big)\Big]r_s^{\frac{n}{2}}-e^{-\varepsilon(\pi-\theta_s)}B\Big[n\cos\Big(\varepsilon$$

$$\ln\frac{r_s}{l}-\frac{n}{2}\theta_s\Big)+2\varepsilon\sin\Big(\varepsilon\ln\frac{r_s}{l}-\frac{n}{2}\theta_s\Big)\Big]r_s^{\frac{n}{2}}\Big\} \quad (5)$$

where $n>0$, n=odd. When $n=1$, Eqs. (1) ~ (5) are stress and displacement fields around the propagating interfacial crack tip. Thus, K_1^o and K_1^* are stress intensity factors K_I and K_{II}. For far field stress σ_y^∞ and τ_{xy}^∞ at infinity, the stress intensity factors K_I and K_{II} are given as

$$K_I+iK_{II}=\sqrt{\pi a}\,(1+2i\varepsilon)\Big(\sigma_y^\infty+i\frac{1}{\eta}\tau_{xy}^\infty\Big) \quad (6)$$

and the energy release rate is given by

$$G=\frac{(K_I^2+K_{II}^2)\,h_{21}}{4\cosh^2(\varepsilon\pi)} \quad (7)$$

The G for a propagating crack in isotropic material becomes infinite when crack tip speed approaches the Rayleigh wave speed but remains finite for an interfacial propagating crack. where

$$A_n^o=\frac{K_n^o}{\sqrt{2\pi}}a^{n/2-1}, \quad A_n^*=\frac{K_n^*}{\sqrt{2\pi}}a^{n/2-1}, \quad \varepsilon=\frac{1}{2\pi}\ln$$

$$\frac{1-\beta}{1+\beta}, \quad \beta=\frac{h_{11}}{\sqrt{h_{12}h_{21}}}$$

$h_{11} = (l_{11})_1 - (l_{11})_2, \quad h_{12} = (l_{12})_1 + (l_{12})_2,$

$h_{21} = (l_{21})_1 + (l_{21})_2, \quad \eta = (h_{21}/h_{12})^{1/2},$

$(l_{11})_1 = \left\{ \dfrac{2\beta_l\beta_s - (1+\beta_s^2)}{\mu D_1} \right\},$

$(l_{12})_1 = \left\{ \dfrac{\beta_s(1-\beta_s^2)}{\mu D_1} \right\}$

$(l_{21})_1 = \left\{ \dfrac{\beta_l(1-\beta_s^2)}{\mu D_1} \right\},$

$(l_{11})_2 = \dfrac{p_s\alpha_l - p_l\alpha_s}{D_2} = \dfrac{q_s - q_l}{\alpha_s - \alpha_l},$

$(l_{12})_2 = \dfrac{(1+M_a)(p_l - p_s)}{D_2}, \quad (l_{21})_2 = \dfrac{\alpha_s q_l - \alpha_l q_s}{D_2},$

$D_1 = [4\beta_l\beta_s - (1+\beta_s^2)^2],$

$D_2 = (1+M_a)(\alpha_s - \alpha_l),$

$\beta_l = \sqrt{1-\left(\dfrac{c}{c_l}\right)^2}, \quad \beta_s = \sqrt{1-\left(\dfrac{c}{c_s}\right)^2},$

$r_l = r\sqrt{1-\left(\dfrac{c}{c_l}\right)^2 \sin^2\theta},$

$r_s = r\sqrt{1-\left(\dfrac{c}{c_s}\right)^2 \sin^2\theta},$

l =crack length ($2a$ for center crack and a for edge crack), and the c, c_l and c_s are the crack propagation velocity, longitudinal and shear wave velocity for material 1 (isotropic material) respectively. Meanwhile, the p_l, p_s, q_l, q_s, α_l, α_s, M_a and the fields for the material below the interface (the orthotropic material) are given in reference (Lee, 1999).

3. The Determination of Stress Intensity Factors by Boundary Collocation

The bimaterial model which was used in this study is shown in Fig. 2 with the traction T_y applied on upper and lower boundaries. In the figure $\tau_{xy}=0$ on $\overline{AB}$, $T_y=\sigma$ on $\overline{BC}$, $\tau_{xy}=0$, $u_x=0$ on $\overline{CD}$, $T_y=\sigma$ on $\overline{DA}$.

Since the loading, material and geometry are symmetric about vertical axis, only one half (right) of the plate is considered. The total number of the selected points along the boundary are 120 (40 along AB, 20 along BC, 40 along CD, 20 along DA). Meanwhile, the stress and displacements of Eqs. (1) ~ (5) can be represented as Eq. (8).

$\sigma_{ij} = \sum_{n=1}^{\infty} (A_n^o H_{ijn}^o + A_n^* H_{ijn}^*), \quad u_i = \sum_{n=1}^{\infty} (A_n^o U_{in}^o + A_n^* U_{in}^*)$ (8)
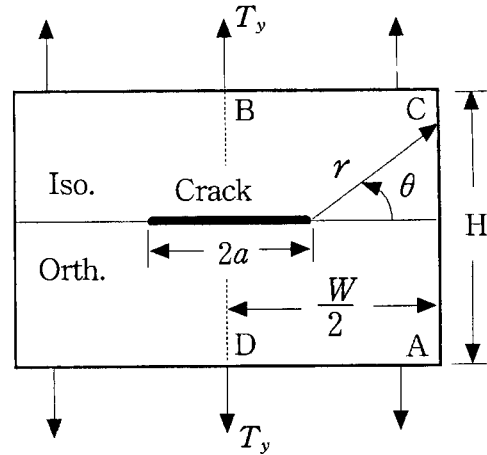
Fig. 2 Model of rectangular isotropic-orthotropic bimaterial plate

where, the H_{ijn}^o, H_{ijn}^*, U_{xn}^o and U_{xn}^* can be obtained from boundary collocation points and material properties. The σ_{yn} and u_{xn} also are known from the boundary collocation points. Thus, A_n^o and A_n^*, which are unknown values, can be obtained from Eq. (8). Therefore, the K_I^o and K_I^*, which are K_I and K_{II}, are respectively, can be obtained from A_n^o and A_n^*. Equation (8) is expanded for n=1, 3, 5, $\cdots$, 59 thus giving us 60 unknown coefficients: A_1^o, $\cdots$, A_{59}^o and A_1^*, $\cdots$, A_{59}^*. When the boundary conditions, material properties and coordinates r, θ of the selected boundary are substituted into the general stress and displacement fields, 120 simultaneous equations with unknown coefficients A_n^o, A_n^* are constructed. The solutions, which satisfy the boundary conditions, are obtained by using least squares method.

If the external traction and elastic properties are symmetric about x-axis, τ_{xy} is zero along the x-axis. Under these circumstances, only the term A_n^o which is related to stress intensity factor K_I is used, and the exact value $K_I (=A_1^o\sqrt{2\pi a})$ can be obtained. For interface crack in bimaterials, although external traction is symmetric about the x-axis, τ_{xy} exists along the x-axis because the elastic properties are not symmetric about x-axis. Under these circumstances, the coefficients A_n^o and A_n^* must be used.

4. Experimental Details and Analysis

4.1 Extraction of fracture parameters from isochromatic fringes

The stress field Eqs. (1) ~ (3) combined with the stress optic law (equation 9) define the order of the isochromatics at any given point around the crack tip.

$$\frac{N}{t} = \frac{1}{f}\sqrt{(\sigma_x - \sigma_y)^2 + (2\tau_{xy})^2} \qquad (9)$$

where N is fringe order, t the thickness of specimen and f the material fringe constant. The fringe order at a selected set of points was obtained from the digital photographs of computer, and the fracture parameters were evaluated from the selected points $(t < r < 3t)$ around crack tip using the non-linear least squares method in conjection with the Newton–Raphson technique (Robert, 1980). The fracture parameters of stationary crack were obtained using the dynamic equations by giving c/c_{s1} a value close to zero.

4.2 Static experiments

A series of experiments was conducted using the center crack geometry having different crack length for two fiber orientations. The two fiber orientations considered were fibers paraller to the interface $(\alpha = 0°)$ and fibers perpendicular to the interface $(\alpha = 90°)$. The bimaterials used to evaluate the fracture parameters consist of the PSM-1 for isotropic material (Mat. 1) and Scotchply –1002 for orthotropic material (Mat. 2). The material properties are shown in Table 1. The width, height and thickness of specimen are 254mm, 508mm and 9.525mm respectively. The bonding faces of the plates were machined to obtain a flat surface, roughened with 400-grit sand paper and thoroughly cleaned with methanol. Teflon tape(25 μm thick) of the required length was used to create the initial crack during bonding process. Epoxy adhesive, having properties same as those of the matrix was used for bonding the two plates in order to obtain a true bimaterial system. During debonding of the bond between PSM and Scothchply under impact

Table 1 Material properties for bimaterials

Property	PSM		Property	Scotchply	
	Stat.	Dyna.		Stat.	Dyna.
E(GPa)	2.50	2.76	E_L	39.3	47.12
			E_T	9.67	13.05
μ(GPa)	.905	1.0	μ_{LT}	3.10	3.89
ν	.38	.35	ν_{LT}	.254	.254
ρ(kg/m³)	1200	1200	ρ	1860	1860
f_σ(kN/m)	6.45	7.0	f_σ	–	–

E : Young's modulus, μ : Shear modulus,
ν : Poisson's ratio, ρ : Density,
f_σ : Material fringe constant, L : Fiber direction,
T : Normal direction to fiber one.

load, the bond membrane sticks on the face of PSM. The fact proves that the PSM and bond are one material which bonded perfectly.

A far field uniform tensile load was applied to the specimen using an Instron machine, and the isochromatics corresponding to load increments of 225 N were recorded using a light field circular polariscope and a digital camera for each crack length and fiber orientation. The experiments were conducted for five crack length corresponding to $2a/W$ ratio varying from 0.2 to 0.6.

4.3 Dynamic experiments

Dynamic fracture experiments were performed for both fiber orientations using the single edge crack geometry. The specimen preparation was identical to that followed for static experiments. The experimental setup shown in Fig. 3 comprised of a high-speed digital carmer, a light field polariscope, the bimaterial and flash light source.

Figure 4 shows the static isochromatic fringe patterns in the PSM for a static center crack in PSM-1/Scotchply-1002 bimaterial. As known, the fringe orders (N=3.5, 4.0, 4.5, 5.0) at crack are greater when $\alpha = 90°$ than when $\alpha = 0°$. The orthotropic material of $\alpha = 0°$ is more compliant than that of $\alpha = 90°$ for loading direction. Thus, it can be inferred that the stress intensity factor at crack tip of the isotropic material bonded with orthotropic material of $\alpha = 90°$ is greater than that bonded with orthotropic material of $\alpha = 0°$ under

same load.

Meanwhile, the isochromatic fringe patterns are normal about crack direction at crack tip. Increasing the r, they tilt to the $(+)x$ direction because of the remote stress σ_{ox} of x direction, where, a value of $\sigma_{ox}>0$ tends to compressive stress along the crack line and $\sigma_{ox}<0$ produces tensile stress. The σ_{ox} increases as the crack tip speed increases, and the σ_{ox} in the stiff material is greater than that in compliant one. The greater the difference of physical properties in two materials, the greater the σ_{ox} in stiff material, and the smaller the σ_{ox} in compliant one. When the crack propagates at high speed, even if the σ_{ox} has high value, the isochromatic fringe patterns at remote zone move to reverse direction of crack
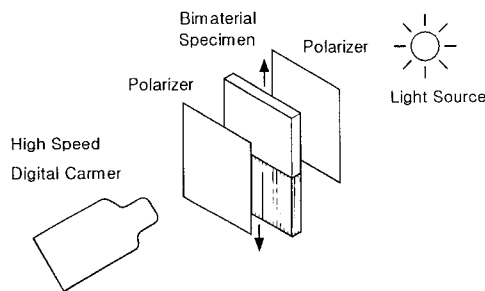
Fig. 3 Experimental setup for investigating the fracture of a bimaterial interface

propagating one.

Figure 5 shows the dynamic isochromatic fringe patterns in the PSM-1 half for an edge crack propagating along the interface of a PSM -1/Scotchply-1002 bimaterial photoed by speed digital carmer (IMACON-200), with which 16 images of the propagating crack were captured.

5. Evaluation of Fracture Parameters

Figure 6 shows the normalized stress intensity factors (NSIFs) obtained from the numerical analysis and the experiments for static crack in PSM-1/Scotchply-1002 bimaterial. The normalized stress intensity factors for $\alpha=0°$ are less than those for $\alpha=90°$ which are very close to those of isotropic material. As the normalized crack length approaches to 0.2, the normalized stress intensity factors approach to 1.0095, which is a good agreement with the results from Eq. (6) for stationary crack. Generally, the normalized stress intensity factor for embedded cracks aligned normal to fibers is greater than those of crack aligned with fiber (Lee et al., 1999). It can be identified that NSIFs for the isotropic -orthotropic bimaterial also show the same tendency as those of orthotropic materials.
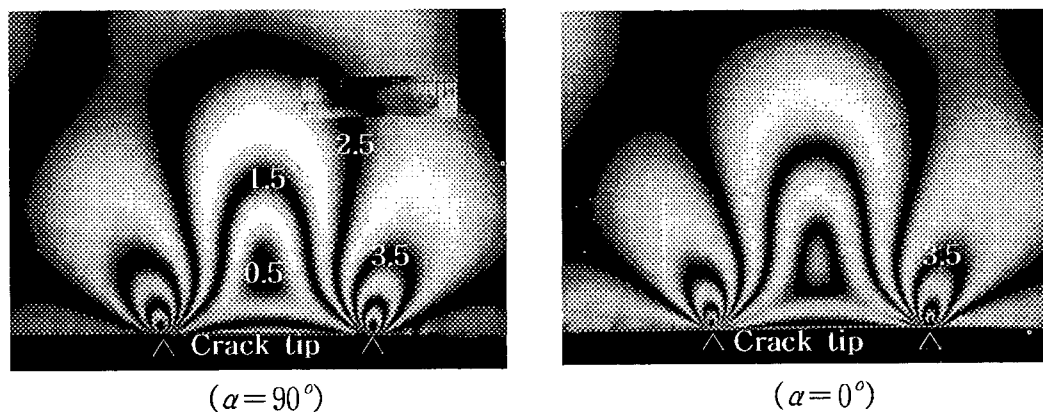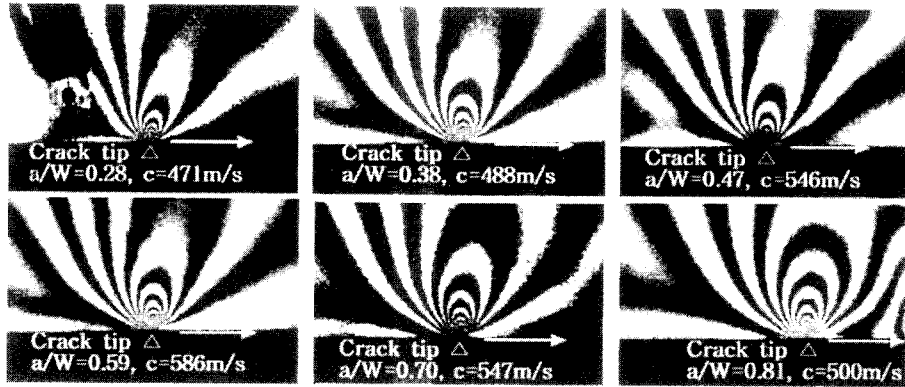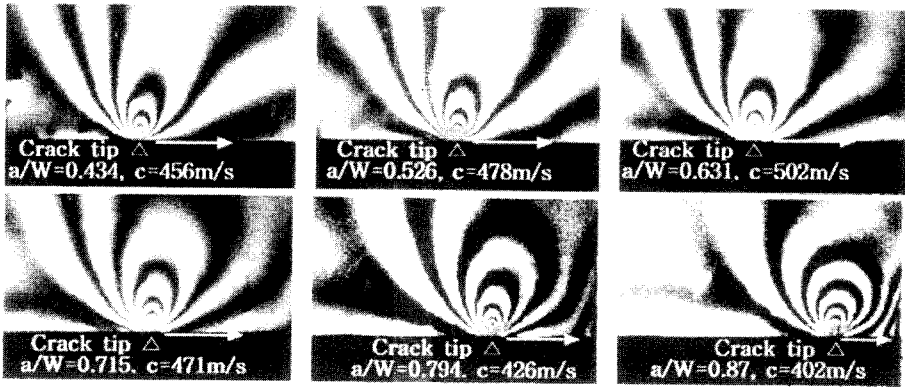

$(\alpha=90°)$ $(\alpha=0°)$

Fig. 4 Isochromatic fringe patterns for a static center crack in PSM/Scotchply bimaterial photoed by digital carmer. $2a/W=0.3$, Load$=3.56$KN, W$=254$mm, t$=9.525$mm, H/W$=2$

Fig. 5 Isochromatic fringe patterns for a propagating crack in PSM/Scotchply bimaterial photoed by high-speed digital carmer
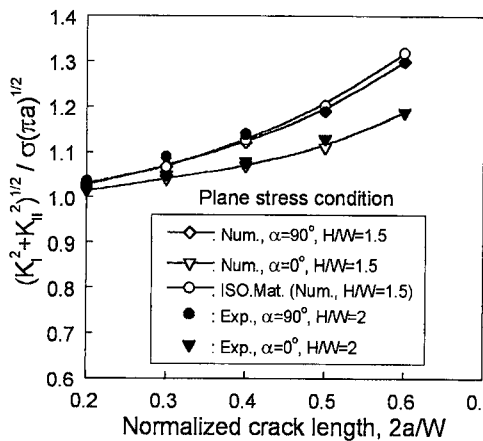

Fig. 6 The $\sqrt{K_I^2 + K_{II}^2}/\sigma\sqrt{\pi a}$ with normalized crack length for static load
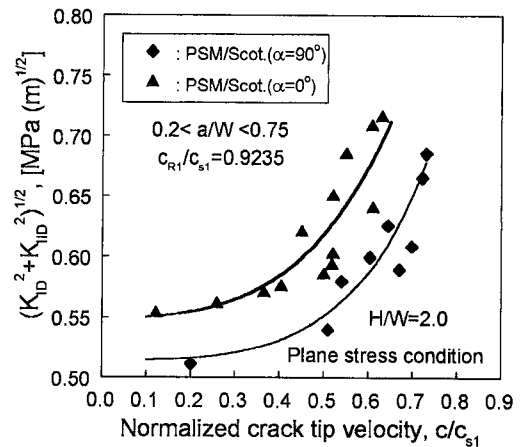

Fig. 7 The $\sqrt{K_{ID}^2 + K_{IID}^2}$ with normalized crack length for a propagating crack
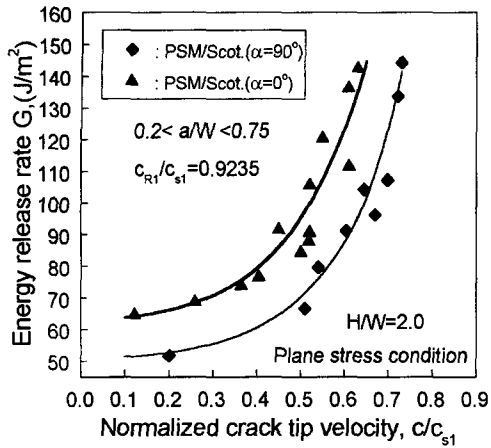
Fig. 8   The energy release rate G with normalized crack length for a propagating crack
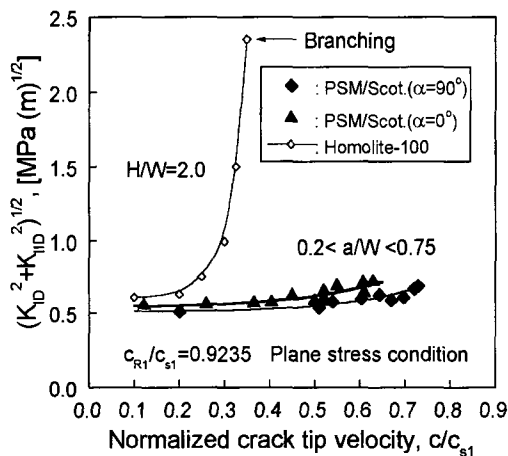

Fig. 9   The comparison of dynamic stress intensity factors between an isotropic material and an isotropic-orthotropic bimaterial for a propagating crack

Figure 7 shows the amplitude of dynamic complex stress intensity factor, $|K_D|$, as a function of the normalized crack speed for propagating interfacial crack for both fiber orientations ($\alpha=0°$ and $\alpha=90°$). As opposed to the stationary crack, the $|K_D|$ values are higher when the fibers are aligned parallel to the interface ($\alpha=0°$). When the fibers are perpendicular to the interface, the ends of the fibers meeting the interface act as weak spots in the path of the propagating crack resulting in smaller values of the $|K_D|$. The $|K_D|$ versus c relationship for bi-materials having high

mismatch, proposed by Kavaturu and Shukla (Kavaturu et al., 1998), indicates that the $|K_D|$ initially increased with crack velocity and then decreases and remains finite as the crack velocity approaches the Rayleigh wave speed of the more compliant material. Especially, the decrease in $|K_D|$ occurs in the velocity range of $0.8 < c/c_{s1} < 0.9$, under shear dominated crack growth (Kavaturu et al., 1998). The $|K_D|$ in the present study registers an increasing trend with increasing crack velocity for the velocity ranges observed. This is could be due to the low mismatch levels ($\varepsilon=0.07\sim0.14$) and opening mode dominated nature of the crack growth. As shown in Fig. 9, even though the $|K_D|$ vs c relationship is similar to that for isotropic homogeneous materials (Homolite-100), the rate of increase of G or $|K_D|$ with crack speed is not as drastic as that reported for homogeneous materials (Kobayashi et al., 1977). Hence, further experimental data in the high velocity regime is necessary to confirm this similarity.

The energy release rate G, as a function of normalized crack speed, shown in Fig. 8, also indicate the same trend as the $|K_D|$. The dynamic energy release rate for an isotropic material increases rapidly with crack propagation velocity, and becomes infinite value when a crack velocity approaches the Rayleigh wave speed. It causes the crack to branch at low velocity. But the dynamic energy release rate for an interfacial propagating crack of bimaterial increases slowly with crack propagation velocity, and remains finite for the velocity ranges observed in this study.

Figure 10 shows the comparison of theoretical isochromatic fringes between the $\alpha=90°$ and the $\alpha=0°$ by stress-optic law combined with the stress fields. The theoretical isochromatic fringe patterns for static crack and propagating crack are similar to the experimental isochromatic fringe ones (Fig. 4, Fig. 5). The stress intensity factors for static crack obtained in this study are greater when $\alpha=90°$ than when $\alpha=0°$ but the dynamic stress intensity factors are reverse. It can be inferred that the actual fringe ratio r/r' for static crack is somewhat greater than 1.19 and for propagating crack, it is somewhat less than 1.86.
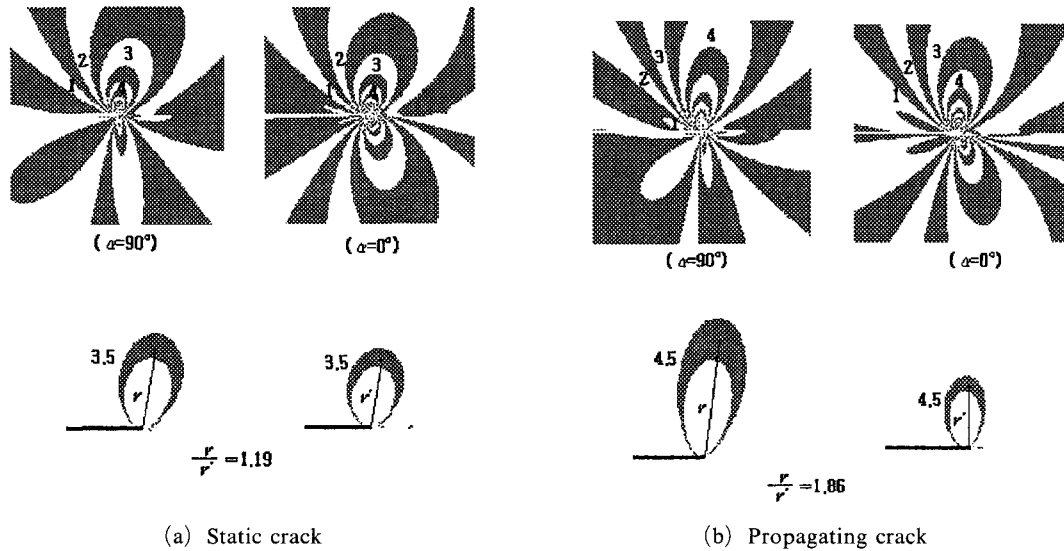
(α=90°)   (α=0°)   (α=90°)   (α=0°)

$\dfrac{r}{r'}$ =1.19 $\dfrac{r}{r'}$ =1.86

(a) Static crack   (b) Propagating crack

Fig. 10   The comparison of theoretical isochromatic fringes between the $a=90°$ and the $a=0°$ by stress optic law. $K_I/\sigma\sqrt{\pi a}=1.05$, $K_{II}/\sigma\sqrt{\pi a}=0.15$, $K_2^o=2.6\text{Mpa}$, $2a/W=0.3$, Load$=3.56$KN for static crack and $K_I=0.6\text{MPa}(\text{m})^{1/2}$, $K_{II}=0.15\text{MPa}(\text{m})^{1/2}$, $K_2^o(\sigma_{ox}$ parameter$)=7.58\text{MPa}$, $a=0.127\text{m}$, $c=547\text{m/s}$ for propagating crack

5. Conclusions

The fracture parameters for isotropic -orthotropic bimaterial are studied for interfacial static and dynamic crack under opening mode load. It is confirmed from numerical and experimental method that the normalized stress intensity factors for static crack is greater when $a=90°$ than when $a=0°$, and those when $a=90°$ are similar to ones of isotropic material. The dynamic stress intensity factors for interfacial propagating crack are greater when $a=0°$ than $a=90°$. It can be inferred that the bonding force at interface is greater when $a=0°$ than when $a= 90°$. For the velocity ranges $(0.1 < c/c_{s1} < 0.7)$ observed in this study, the complex dynamic stress intensity factor $|K_D|$ increases with crack speed c, however, the rate of increase of $|K_D|$ with crack speed is not as drastic as that reported for homogeneous materials.

Acknowledgement

Reference

Deng, X., 1993, "General Crack-Tip Fields for Stationary and Steadily Growing Interface Cracks in Anisotropic Bimaterials," *J. of Appl. Mech.*, Vol. 60, pp. 183~189.

Gdoutos, E. E. and Papakaliatakis, 1982, "Photoelastic Study of a Bimaterial Plate with a Crack Along the Interface," *Engng. Fract. Mech.* Vol. 16, No. 2, pp. 177~182.

Kavaturu, M. and Shukla, A., 1998, "Dynamic Fracture Criteria for Crack Growth Along Bimaterial Interfaces," *J. of Appl. Mech.*, Vol. 65, pp. 293~299.

Kobayashi, T. and Dally, J. W, 1977, "The relation Between Crack Velocity and Sress Intensity Factor in Birefringent Polymers, Fast Fracture and Crack Arrest," *ASTM STP* 627, 257 ~273.

Lambros J. and Rosakis, A. J., 1995a, "Development a Dynamic Decohesion Criterion for Subsonic Fracture of the Interface Between Two Dissimilar Materials," *Proc. R. Soc. Lond.* (A),

451, pp. 711~736.

Lambros J. and Rosakis, A. J., 1995b, "Dynamic decohesion of Bimaterial: Experimental Observation and Failure Criteria," *Int. J. Solids Struct.*, Vol. 32, No. 17, 18, pp. 2677 ~2702.

Lee, K. H., 1999, "Stress and Displacement Fields for Propagating Crack along Interface of Isotropic-Orthotropic Material under Dynamic Mode I and II Load," *Transactions of the KSME* (*A*), Vol. 23, No. 9, pp. 1463~1475.

Lee, K. H. and Choi, Y. C., 1999, "Analysis of Propagating Flat Crack in Orthotropic Rectan-gular Plate," *Transactions of the KSME* (*A*), Vol. 23, No. 1, pp. 89~98.

Lu, H. and Chiang F. P., 1993, "Photoelastic Determination of Stress Intensity Factor of an Interfacial Crack in a Bi-material," *J. of Appl. Mech.*, Vol. 60, pp. 93~100.

Robert, J. S., 1980, "Application of the Least Square Method to Photoelastic Analysis," *Exp. Mech.* pp. 192~197.

Yang, W., Suo, Z. and Shih, C. F., 1991, "Mechanics of Dynamic Debonding," *Proc., R. Soc. of Lond*, A. 433, pp. 679~697.